

1 **A LOCALLY DIVERGENCE-FREE LOCAL CHARACTERISTIC DECOMPOSITION**
2 **BASED PATH-CONSERVATIVE CENTRAL-UPWIND SCHEME FOR IDEAL**
3 **MAGNETOHYDRODYNAMICS***

4 SHAOSHUAI CHU[†], ALEXANDER KURGANOV[‡], MÁRIA LUKÁČOVÁ-MEDVID'OVÁ[§], AND MINGYE NA[¶]

5 **Abstract.** We introduce a locally divergence-free local characteristic decomposition based path-conservative central-
6 upwind (LCD-PCCU) scheme for ideal magnetohydrodynamics (MHD) equations. The proposed method is a low-dissipation
7 extension of the recently proposed locally divergence-free PCCU scheme. To reduce the numerical dissipation, we incorporate
8 the LCD into the PCCU framework. The resulting LCD-PCCU method enhances the resolution of numerical solutions as
9 demonstrated through a series of benchmark tests.

10 **Key words.** Ideal magnetohydrodynamics, divergence-free constraints, local characteristic decomposition,
11 path-conservative central-upwind scheme.

12 **MSC codes.** 65M08, 76W05, 76M12, 35L65

13 **1. Introduction.** This paper focuses on the development of a novel and low-dissipation numerical
14 method for ideal magnetohydrodynamics (MHD) equations, which play a central role in modeling a wide
15 range of physical phenomena in astrophysics, plasma physics, space physics, and engineering. These mod-
16 els describe the dynamics of electrically conducting fluids interacting with magnetic fields and consist of
17 hyperbolic systems of partial differential equations (PDEs) that couple fluid flow with electromagnetic
18 effects. A crucial property of these models is a constraint on the magnetic field, which has to remain
19 divergence-free if it is divergence-free initially. Numerically, however, this condition is nontrivial to main-
20 tain, and improperly handling the divergence-free constraint at the discrete level can lead to numerical
21 instabilities or the development of nonphysical structures in the solution; see, e.g., [3, 4, 25, 36].

22 Over the past decades, numerous approaches have been developed to address the divergence-free
23 constraint. Among them are the projection method (see, e.g., [4]), the constrained transport (CT) method
24 (see, e.g., [3, 11, 15, 17, 19, 23, 29, 35, 37]), locally divergence-free discontinuous Galerkin [25, 38] and finite-
25 volume [9, 10] methods (these methods maintain zero divergence within each computational cell), and
26 globally divergence-free high-order finite-volume and discontinuous Galerkin methods; see, e.g., [1, 2, 16,
27 18, 26, 27].

28 Alternatively, instead of enforcing the divergence-free constraint explicitly, one can reduce divergence
29 errors through the inclusion of additional Godunov-Powell terms. This leads to the so-called eight-wave
30 formulation of the ideal MHD equations; see, e.g., [20, 31–33]. This formulation introduces nonconservative
31 source terms proportional to the divergence of the magnetic field. Although these terms vanish analytically,
32 they help to control numerical divergence errors by advecting them with the flow and preventing their
33 accumulation. Moreover, the modified system gains important properties such as Galilean invariance
34 and entropy symmetrizability, making it well-suited for the development of entropy-stable schemes; see,

*Submitted to the editors DATE.

Funding: The work of S. Chu was funded by the DFG–SPP 2183: Eigenschaftsgeregelte Umformprozesse with the Project(s) HE5386/19-2,19-3 Entwicklung eines flexiblen isothermen Reckschmiedeprozesses für die eigenschaftsgeregelte Herstellung von Turbinenschaufeln aus Hochtemperaturwerkstoffen (424334423) and by the Deutsche Forschungsgemeinschaft (DFG, German Research Foundation)–SPP 2410 Hyperbolic Balance Laws in Fluid Mechanics: Complexity, Scales, Randomness (CoScaRa) within the Project(s) HE5386/27-1 (Zufällige kompressible Euler Gleichungen: Numerik und ihre Analysis, 525853336). The work of A. Kurganov was supported in part by NSFC grants 12171226 and W2431004. The work of M. Lukáčová-Medviďová was supported by the Deutsche Forschungsgemeinschaft (DFG, German Research Foundation)–SPP 2410 within the Projects LU1470/10-1 (Random Euler Equations and their Numerical Analysis, 525800857), and partially by the Gutenberg Research College and by the DFG - project number 233630050 - TRR 146. She is grateful to the Mainz Institute of Multiscale Modelling for supporting her research.

[†]Department of Mathematics, RWTH Aachen University, Aachen, 52056, Germany (chu@igpm.rwth-aachen.de).

[‡]Department of Mathematics and Shenzhen International Center for Mathematics, Southern University of Science and Technology, Shenzhen, 518055, China (alexander@sustech.edu.cn).

[§]Institute of Mathematics, Johannes Gutenberg University Mainz, Staudingerweg 9, 55128 Mainz, Germany (lukacova@uni-mainz.de).

[¶]Department of Mathematics, Southern University of Science and Technology, Shenzhen, 518055, China and Institute of Mathematics, Johannes Gutenberg University Mainz, Staudingerweg 9, 55128 Mainz, Germany (namingye@uni-mainz.de).

35 e.g., [7, 14, 28, 31–33].

36 In [9], the Godunov-Powell modification of the ideal MHD and shallow water MHD equations was
 37 utilized to develop a locally divergence-free second-order semi-discrete path-conservative central-upwind
 38 (PCCU) scheme, which was later extended to the magnetic rotating shallow water model in [10]. In [9],
 39 the studied systems were augmented by evolution equations for the spatial derivatives of the magnetic field
 40 components, and the resulting systems were numerically solved by a PCCU scheme, which was originally
 41 developed in [6] as a “black-box” solver for general nonconservative hyperbolic systems. We stress that
 42 the PCCU schemes are, like any central and central-upwind (CU) schemes, Riemann-problem-solver-free,
 43 and at the same time, they are designed to handle the nonconservative product terms across cell interfaces
 44 in a stable manner.

45 Although the PCCU scheme for the ideal MHD system [9] is quite accurate, efficient, and robust, its
 46 resolution can be further improved by reducing the amount of numerical dissipation. This can be done
 47 with the help of the local characteristic decomposition (LCD) based PCCU (LCD-PCCU) scheme, which
 48 was recently introduced in [12] as an extension of the LCD-based CU (LCD-CU) scheme proposed in [8]
 49 for hyperbolic systems of conservation laws. Compared with the CU and PCCU schemes, the LCD-CU
 50 and LCD-PCCU schemes achieve higher resolution by aligning the numerical flux computation with the
 51 characteristic structure of the system; see [8, 12, 13]. In this paper, we develop the LCD-PCCU scheme
 52 for the ideal MHD equations and test it on a number of numerical experiments, which confirm that the
 53 proposed scheme achieves high resolution, while being robust and positivity-preserving, and effectively
 54 maintaining divergence control. The obtained numerical results also demonstrate that the new scheme
 55 outperforms the PCCU scheme from [9].

56 The rest of the paper is organized as follows. In §2, we present the Godunov-Powell modification of
 57 the ideal MHD equations and its augmented form. In §3, we apply the two-dimensional (2-D) LCD-PCCU
 58 scheme for the studied MHD system. Finally, in §4, we present results of several numerical experiments.

59 **2. Ideal MHD Equations.** The ideal MHD equations read as

$$\begin{aligned} \rho_t + \nabla \cdot (\rho \mathbf{u}) &= 0, \\ (2.1) \quad (\rho \mathbf{u})_t + \nabla \cdot \left[\rho \mathbf{u} \mathbf{u}^\top + \left(p + \frac{1}{2} |\mathbf{b}|^2 \right) \mathbf{I} - \mathbf{b} \mathbf{b}^\top \right] &= \mathbf{0}, \\ \mathcal{E}_t + \nabla \cdot \left[\left(\mathcal{E} + p + \frac{1}{2} |\mathbf{b}|^2 \right) \mathbf{u} - \mathbf{b}(\mathbf{u} \cdot \mathbf{b}) \right] &= 0, \\ \mathbf{b}_t - \nabla \times (\mathbf{u} \times \mathbf{b}) &= \mathbf{0}, \end{aligned}$$

60 where t is time, ρ is the density, p is the pressure, $\mathbf{u} = (u, v, w)^\top$ is the fluid velocity, $\mathbf{b} = (b_1, b_2, b_3)^\top$ is
 61 the magnetic field, and \mathcal{E} is the total energy. Additionally, \mathbf{I} is the identity matrix and γ is the ratio of
 62 specific heats. The system (2.1) is completed through the equation of state (EOS)

$$(2.2) \quad \mathcal{E} = \frac{p}{\gamma - 1} + \frac{\rho}{2} |\mathbf{u}|^2 + \frac{1}{2} |\mathbf{b}|^2.$$

63 It is easy to show that provided that the magnetic field is initially divergence-free, then the magnetic field
 64 satisfies

$$(2.3) \quad \nabla \cdot \mathbf{b} = 0.$$

65 In this paper, we will develop a new numerical method for the Godunov-Powell modified ideal MHD
 66 equations, which read as

$$\begin{aligned} (2.4) \quad \rho_t + \nabla \cdot (\rho \mathbf{u}) &= 0, \\ (\rho \mathbf{u})_t + \nabla \cdot \left[\rho \mathbf{u} \mathbf{u}^\top + \left(p + \frac{1}{2} |\mathbf{b}|^2 \right) \mathbf{I} - \mathbf{b} \mathbf{b}^\top \right] &= -\mathbf{b}(\nabla \cdot \mathbf{b}), \\ \mathcal{E}_t + \nabla \cdot \left[\left(\mathcal{E} + p + \frac{1}{2} |\mathbf{b}|^2 \right) \mathbf{u} - \mathbf{b}(\mathbf{u} \cdot \mathbf{b}) \right] &= -(\mathbf{u} \cdot \mathbf{b})(\nabla \cdot \mathbf{b}), \\ \mathbf{b}_t - \nabla \times (\mathbf{u} \times \mathbf{b}) &= -\mathbf{u}(\nabla \cdot \mathbf{b}), \end{aligned}$$

71 which is completed through the EOS (2.2). We stress that the system (2.4), (2.2)—unlike the original
 72 system (2.1)–(2.2)—has a complete set of eight eigenvalues with eight corresponding eigenvectors: This
 73 allows for an LCD and thus for designing an LCD-PCCU scheme.

74 As in [9], we restrict our attention to the 2-D case, where all the quantities of interest depend on
 75 the spatial variables x and y and time t only. In this case, the divergence-free condition (2.3) reads as
 76 $(b_1)_x + (b_2)_y = 0$, and we augment the Godunov-Powell modified ideal MHD system (2.4), (2.2) by adding
 77 the equations for the auxiliary variables $A := (b_1)_x$ and $B := (b_2)_y$:

$$78 \quad (2.5) \quad \begin{aligned} A_t + (uA - b_2 u_y)_x + (vA + b_1 v_x)_y &= 0, \\ B_t + (uB + b_2 u_y)_x + (vB - b_1 v_x)_y &= 0, \end{aligned}$$

79 which are obtained by differentiating the b_1 - and b_2 -equations in (2.1).

80 One can write the system (2.4)–(2.5), (2.2) in the following vector form:

$$81 \quad (2.6) \quad \mathbf{U}_t + \mathbf{F}(\mathbf{U})_x + \mathbf{G}(\mathbf{U})_y = Q^x(\mathbf{U})\mathbf{U}_x + Q^y(\mathbf{U})\mathbf{U}_y,$$

$$82 \quad (2.7) \quad \tilde{\mathbf{U}}_t + \tilde{\mathbf{F}}(\mathbf{W})_x + \tilde{\mathbf{G}}(\mathbf{W})_y = \mathbf{0},$$

83 where

$$84 \quad (2.8) \quad \begin{aligned} \mathbf{U} &= (\rho, \rho u, \rho v, \rho w, b_1, b_2, b_3, \mathcal{E})^\top, \quad \tilde{\mathbf{U}} = (A, B)^\top, \quad \mathbf{W} = (\mathbf{U}^\top, \tilde{\mathbf{U}}^\top)^\top, \\ \mathbf{F}(\mathbf{U}) &= \left(\rho u, \rho u^2 + p + \frac{1}{2}|\mathbf{b}|^2 - b_1^2, \rho u v - b_1 b_2, \rho u w - b_1 b_3, 0, u b_2 - v b_1, \right. \\ &\quad \left. u b_3 - w b_1, \left(\mathcal{E} + p + \frac{1}{2}|\mathbf{b}|^2 \right) u - (\mathbf{u} \cdot \mathbf{b}) b_1 \right)^\top, \\ \mathbf{G}(\mathbf{U}) &= \left(\rho v, \rho u v - b_1 b_2, \rho v^2 + p + \frac{1}{2}|\mathbf{b}|^2 - b_2^2, \rho v w - b_2 b_3, v b_1 - u b_2, 0, \right. \\ &\quad \left. v b_3 - w b_2, \left(\mathcal{E} + p + \frac{1}{2}|\mathbf{b}|^2 \right) v - (\mathbf{u} \cdot \mathbf{b}) b_2 \right)^\top, \\ Q^x(\mathbf{U}) &= \mathbf{q}\mathbf{e}_5^\top, \quad Q^y(\mathbf{U}) = \mathbf{q}\mathbf{e}_6^\top, \quad \mathbf{q} := -(0, b_1, b_2, b_3, u, v, w, \mathbf{u} \cdot \mathbf{b})^\top, \\ \tilde{\mathbf{F}}(\mathbf{W}) &= \left(u A - b_2 u_y, u B + b_2 u_y \right)^\top, \quad \tilde{\mathbf{G}}(\mathbf{W}) = \left(v A + b_1 v_x, v B - b_1 v_x \right)^\top, \end{aligned}$$

85 and \mathbf{e}_5 and \mathbf{e}_6 are the fifth and sixth unit vectors in \mathbb{R}^8 , respectively.

86 Note that for smooth solutions, the system (2.4), (2.2) can be rewritten in an equivalent quasi-linear
 87 form:

$$88 \quad (2.9) \quad \mathbf{U}_t + C^x(\mathbf{U})\mathbf{U}_x + C^y(\mathbf{U})\mathbf{U}_y = \mathbf{0},$$

89 where the matrices $C^x(\mathbf{U})$ and $C^y(\mathbf{U})$ are specified in Appendix A. Furthermore, one can switch to the
 90 primitive variables $\mathbf{V} = (\rho, u, v, w, p, b_1, b_2, b_3)^\top$ and rewrite the system (2.9) in a different quasi-linear
 91 form:

$$92 \quad (2.10) \quad \mathbf{V}_t + D^x(\mathbf{V})\mathbf{V}_x + D^y(\mathbf{V})\mathbf{V}_y = \mathbf{0},$$

93 where the matrices $D^x(\mathbf{V})$ and $D^y(\mathbf{V})$ are specified in Appendix B. In the following, we will use the forms
 94 (2.9) and (2.10) to design the LCD-CU numerical fluxes and to perform a piecewise linear reconstruction,
 95 respectively.

96 **3. 2-D Flux Globalization Based LCD-PCCU Scheme.** In this section, we apply the 2-D flux
 97 globalization based LCD-PCCU scheme from [12] to the studied augmented ideal MHD system (2.6)–(2.8).
 98 To this end, we first rewrite the system (2.6) in the following quasi-conservative form:

$$99 \quad (3.1) \quad \mathbf{U}_t + \mathbf{K}(\mathbf{U})_x + \mathbf{L}(\mathbf{U})_y = \mathbf{0}, \quad \mathbf{K}(\mathbf{U}) = \mathbf{F}(\mathbf{U}) - \mathbf{I}^x(\mathbf{U}), \quad \mathbf{L}(\mathbf{U}) = \mathbf{G}(\mathbf{U}) - \mathbf{I}^y(\mathbf{U}),$$

100 where

$$101 \quad \mathbf{I}^x(\mathbf{U}) := \int_{\hat{x}}^x [Q^x(\mathbf{U})\mathbf{U}_\xi(\xi, y, t)] d\xi, \quad \mathbf{I}^y(\mathbf{U}) := \int_{\hat{y}}^y [Q^y(\mathbf{U})\mathbf{U}_\eta(x, \eta, t)] d\eta,$$

102 with \hat{x} and \hat{y} being arbitrary numbers.

We cover the computational domain with uniform cells $C_{j,k} := [x_{j-\frac{1}{2}}, x_{j+\frac{1}{2}}] \times [y_{k-\frac{1}{2}}, y_{k+\frac{1}{2}}]$ centered at $(x_j, y_k) = ((x_{j-\frac{1}{2}} + x_{j+\frac{1}{2}})/2, (y_{k+\frac{1}{2}} + y_{k-\frac{1}{2}})/2)$ with $x_{j+\frac{1}{2}} - x_{j-\frac{1}{2}} \equiv \Delta x$ and $y_{k+\frac{1}{2}} - y_{k-\frac{1}{2}} \equiv \Delta y$ for $j = 1, \dots, N_x$, $k = 1, \dots, N_y$, and assume that the computed cell averages of \mathbf{W} over the corresponding cells $C_{j,k}$,

$$\overline{\mathbf{W}}_{j,k}(t) \approx \frac{1}{\Delta x \Delta y} \int_{C_{j,k}} \mathbf{W}(x, y, t) dx dy,$$

103 are available at a certain time level $t \geq 0$. Note that $\overline{\mathbf{W}}_{j,k}$ as well as many of the indexed quantities
104 introduced below are time-dependent, but from here on, we suppress this dependence for the sake of
105 brevity.

106 According to [12], the cell averages $\overline{\mathbf{W}}_{j,k} = (\overline{\mathbf{U}}_{j,k}^\top, \overline{\tilde{\mathbf{U}}}_{j,k}^\top)^\top$ are evolved in time by numerically solving
107 the following system of ODEs:

$$108 \quad (3.2) \quad \begin{aligned} \frac{d\overline{\mathbf{U}}_{j,k}}{dt} &= -\frac{\mathcal{K}_{j+\frac{1}{2},k}^{\text{LCD}} - \mathcal{K}_{j-\frac{1}{2},k}^{\text{LCD}}}{\Delta x} - \frac{\mathcal{L}_{j,k+\frac{1}{2}}^{\text{LCD}} - \mathcal{L}_{j,k-\frac{1}{2}}^{\text{LCD}}}{\Delta y}, \\ \frac{d\overline{\tilde{\mathbf{U}}}_{j,k}}{dt} &= -\frac{\tilde{\mathcal{F}}_{j+\frac{1}{2},k} - \tilde{\mathcal{F}}_{j-\frac{1}{2},k}}{\Delta x} - \frac{\tilde{\mathcal{G}}_{j,k+\frac{1}{2}} - \tilde{\mathcal{G}}_{j,k-\frac{1}{2}}}{\Delta y}, \end{aligned}$$

109 where the numerical fluxes $\tilde{\mathcal{F}}_{j+\frac{1}{2},k}$ and $\tilde{\mathcal{G}}_{j,k+\frac{1}{2}}$ are evaluated by the CU scheme from [24]

$$110 \quad (3.3) \quad \begin{aligned} \tilde{\mathcal{F}}_{j+\frac{1}{2},k} &= \frac{s_{j+\frac{1}{2},k}^+ \tilde{\mathbf{F}}(\mathbf{W}_{j,k}^E) - s_{j+\frac{1}{2},k}^- \tilde{\mathbf{F}}(\mathbf{W}_{j+1,k}^W)}{s_{j+\frac{1}{2},k}^+ - s_{j+\frac{1}{2},k}^-} + \frac{s_{j+\frac{1}{2},k}^+ s_{j+\frac{1}{2},k}^-}{s_{j+\frac{1}{2},k}^+ - s_{j+\frac{1}{2},k}^-} (\tilde{\mathbf{U}}_{j+1,k}^W - \tilde{\mathbf{U}}_{j,k}^E), \\ \tilde{\mathcal{G}}_{j,k+\frac{1}{2}} &= \frac{s_{j,k+\frac{1}{2}}^+ \tilde{\mathbf{G}}(\mathbf{W}_{j,k}^N) - s_{j,k+\frac{1}{2}}^- \tilde{\mathbf{G}}(\mathbf{W}_{j,k+1}^S)}{s_{j,k+\frac{1}{2}}^+ - s_{j,k+\frac{1}{2}}^-} + \frac{s_{j,k+\frac{1}{2}}^+ s_{j,k+\frac{1}{2}}^-}{s_{j,k+\frac{1}{2}}^+ - s_{j,k+\frac{1}{2}}^-} (\tilde{\mathbf{U}}_{j,k+1}^S - \tilde{\mathbf{U}}_{j,k}^N), \end{aligned}$$

111 the global numerical fluxes $\mathcal{K}_{j+\frac{1}{2},k}^{\text{LCD}}$ and $\mathcal{L}_{j,k+\frac{1}{2}}^{\text{LCD}}$ are given by

$$112 \quad (3.4) \quad \begin{aligned} \mathcal{K}_{j+\frac{1}{2},k}^{\text{LCD}} &= R_{j+\frac{1}{2},k}^x P_{j+\frac{1}{2},k}^{\text{LCD}} (R_{j+\frac{1}{2},k}^x)^{-1} \mathbf{K}_{j,k}^E + R_{j+\frac{1}{2},k}^x M_{j+\frac{1}{2},k}^{\text{LCD}} (R_{j+\frac{1}{2},k}^x)^{-1} \mathbf{K}_{j+1,k}^W \\ &\quad + R_{j+\frac{1}{2},k}^x Q_{j+\frac{1}{2},k}^{\text{LCD}} (R_{j+\frac{1}{2},k}^x)^{-1} (\mathbf{U}_{j+1,k}^W - \mathbf{U}_{j,k}^E), \\ \mathcal{L}_{j,k+\frac{1}{2}}^{\text{LCD}} &= R_{j,k+\frac{1}{2}}^y P_{j,k+\frac{1}{2}}^{\text{LCD}} (R_{j,k+\frac{1}{2}}^y)^{-1} \mathbf{L}_{j,k}^N + R_{j,k+\frac{1}{2}}^y M_{j,k+\frac{1}{2}}^{\text{LCD}} (R_{j,k+\frac{1}{2}}^y)^{-1} \mathbf{L}_{j,k+1}^S \\ &\quad + R_{j,k+\frac{1}{2}}^y Q_{j,k+\frac{1}{2}}^{\text{LCD}} (R_{j,k+\frac{1}{2}}^y)^{-1} (\mathbf{U}_{j,k+1}^S - \mathbf{U}_{j,k}^N), \end{aligned}$$

113 and the global fluxes $\mathbf{K}_{j,k}^{\text{E,W}}$ and $\mathbf{L}_{j,k}^{\text{N,S}}$ in (3.4) are obtained using (3.1):

$$114 \quad (3.5) \quad \mathbf{K}_{j,k}^{\text{E,W}} = \mathbf{F}(\mathbf{U}_{j,k}^{\text{E,W}}) - (\mathbf{I}^x)_{j,k}^{\text{E,W}}, \quad \mathbf{L}_{j,k}^{\text{N,S}} = \mathbf{G}(\mathbf{U}_{j,k}^{\text{N,S}}) - (\mathbf{I}^y)_{j,k}^{\text{N,S}}.$$

115 In (3.3)–(3.5), the following quantities have been used.

• $\mathbf{U}_{j,k}^{\text{E,W,N,S}}$ are the point values of \mathbf{U} at midpoints of the cell interfaces of $C_{j,k}$. They are obtained using a piecewise linear reconstruction applied to the primitive variables \mathbf{V} using the corresponding LCD. To this end, we first compute

$$\begin{aligned} u_{j,k} &= \frac{(\rho u)_{j,k}}{\bar{\rho}_{j,k}}, \quad v_{j,k} = \frac{(\rho v)_{j,k}}{\bar{\rho}_{j,k}}, \quad w_{j,k} = \frac{(\rho w)_{j,k}}{\bar{\rho}_{j,k}}, \\ p_{j,k} &= (\gamma - 1) \left[\bar{\mathcal{E}}_{j,k} - \frac{\bar{\rho}_{j,k}}{2} (u_{j,k}^2 + v_{j,k}^2 + w_{j,k}^2) - \frac{1}{2} ((\bar{b}_1)_{j,k}^2 + (\bar{b}_2)_{j,k}^2 + (\bar{b}_3)_{j,k}^2) \right], \end{aligned}$$

116 where the latter expression has been obtained using the EOS (2.2).

We then switch to the local characteristic variables $\boldsymbol{\Gamma}$ at the midpoints of each of the cell interfaces $(x_{j+\frac{1}{2}}, y_k)$ and $(x_j, y_{k+\frac{1}{2}})$:

$$\begin{aligned}\boldsymbol{\Gamma}_{\ell,k}^x &= \left(T_{j+\frac{1}{2},k}^x\right)^{-1} \mathbf{V}_{\ell,k}, \quad \ell = j-1, j, j+1, j+2, \\ \boldsymbol{\Gamma}_{j,m}^y &= \left(T_{j,k+\frac{1}{2}}^y\right)^{-1} \mathbf{V}_{j,m}, \quad m = k-1, k, k+1, k+2,\end{aligned}$$

where the matrices $T_{j+\frac{1}{2},k}^x$ and $T_{j,k+\frac{1}{2}}^y$ are obtained using the LCD for the primitive system (2.10) and they are given in Appendix B.

Next, we perform generalized minmod reconstructions in the x - and y -directions to evaluate the slopes

120

$$\begin{aligned}(3.6) \quad (\boldsymbol{\Gamma}_x^x)_{j,k} &= \text{minmod}\left(\theta \frac{\boldsymbol{\Gamma}_{j+1,k}^x - \boldsymbol{\Gamma}_{j,k}^x}{\Delta x}, \frac{\boldsymbol{\Gamma}_{j+1,k}^x - \boldsymbol{\Gamma}_{j-1,k}^x}{2\Delta x}, \theta \frac{\boldsymbol{\Gamma}_{j,k}^x - \boldsymbol{\Gamma}_{j-1,k}^x}{\Delta x}\right), \\ (\boldsymbol{\Gamma}_x^x)_{j+1,k} &= \text{minmod}\left(\theta \frac{\boldsymbol{\Gamma}_{j+2,k}^x - \boldsymbol{\Gamma}_{j+1,k}^x}{\Delta x}, \frac{\boldsymbol{\Gamma}_{j+2,k}^x - \boldsymbol{\Gamma}_{j,k}^x}{2\Delta x}, \theta \frac{\boldsymbol{\Gamma}_{j+1,k}^x - \boldsymbol{\Gamma}_{j,k}^x}{\Delta x}\right),\end{aligned}$$

and

$$\begin{aligned}(3.7) \quad (\boldsymbol{\Gamma}_y^y)_{j,k} &= \text{minmod}\left(\theta \frac{\boldsymbol{\Gamma}_{j,k+1}^y - \boldsymbol{\Gamma}_{j,k}^y}{\Delta y}, \frac{\boldsymbol{\Gamma}_{j,k+1}^y - \boldsymbol{\Gamma}_{j,k-1}^y}{2\Delta y}, \theta \frac{\boldsymbol{\Gamma}_{j,k}^y - \boldsymbol{\Gamma}_{j,k-1}^y}{\Delta y}\right), \\ (\boldsymbol{\Gamma}_y^y)_{j,k+1} &= \text{minmod}\left(\theta \frac{\boldsymbol{\Gamma}_{j,k+2}^y - \boldsymbol{\Gamma}_{j,k+1}^y}{\Delta y}, \frac{\boldsymbol{\Gamma}_{j,k+2}^y - \boldsymbol{\Gamma}_{j,k}^y}{2\Delta y}, \theta \frac{\boldsymbol{\Gamma}_{j,k+1}^y - \boldsymbol{\Gamma}_{j,k}^y}{\Delta y}\right),\end{aligned}$$

respectively. In (3.6) and (3.7), the minmod function is defined as

$$\text{minmod}(z_1, z_2, \dots) := \begin{cases} \min_j \{z_j\} & \text{if } z_j > 0 \quad \forall j, \\ \max_j \{z_j\} & \text{if } z_j < 0 \quad \forall j, \\ 0 & \text{otherwise,} \end{cases}$$

and it is applied in a component-wise manner. The parameter $\theta \in [1, 2]$ is used to control the non-oscillatory property of the resulting scheme: larger θ typically leads to a sharper, but more oscillatory computed solution.

We then evaluate the corresponding one-sided point values:

$$\begin{aligned}(\boldsymbol{\Gamma}_{j,k}^x)^E &= \boldsymbol{\Gamma}_{j,k}^x + \frac{\Delta x}{2} (\boldsymbol{\Gamma}_x^x)_{j,k}, \quad (\boldsymbol{\Gamma}_{j+1,k}^x)^W = \boldsymbol{\Gamma}_{j+1,k}^x - \frac{\Delta x}{2} (\boldsymbol{\Gamma}_x^x)_{j+1,k}, \\ (\boldsymbol{\Gamma}_{j,k}^y)^N &= \boldsymbol{\Gamma}_{j,k}^y + \frac{\Delta y}{2} (\boldsymbol{\Gamma}_y^y)_{j,k}, \quad (\boldsymbol{\Gamma}_{j,k+1}^y)^S = \boldsymbol{\Gamma}_{j,k+1}^y - \frac{\Delta y}{2} (\boldsymbol{\Gamma}_y^y)_{j,k+1},\end{aligned}$$

switch back to the primitive variables:

$$\mathbf{V}_{j,k}^E = T_{j+\frac{1}{2},k}^x (\boldsymbol{\Gamma}_{j,k}^x)^E, \quad \mathbf{V}_{j+1,k}^W = T_{j+\frac{1}{2},k}^x (\boldsymbol{\Gamma}_{j+1,k}^x)^W, \quad \mathbf{V}_{j,k}^N = T_{j,k+\frac{1}{2}}^y (\boldsymbol{\Gamma}_{j,k}^y)^N, \quad \mathbf{V}_{j,k+1}^S = T_{j,k+\frac{1}{2}}^y (\boldsymbol{\Gamma}_{j,k+1}^y)^S,$$

and then transform $\mathbf{V}_{j,k}^{E,W,N,S}$ into $\mathbf{U}_{j,k}^{E,W,N,S}$, which are non-oscillatory, but they do not necessarily satisfy the local divergence-free requirement, which can be written as

131

$$(3.8) \quad (\boldsymbol{\nabla} \cdot \mathbf{b})_{j,k} := \frac{(b_1)_{j,k}^E - (b_1)_{j,k}^W}{\Delta x} + \frac{(b_2)_{j,k}^N - (b_2)_{j,k}^S}{\Delta y} \equiv 0, \quad \forall j, k.$$

We thus need to correct the point values $(b_1)_{j,k}^{E,W}$ and $(b_2)_{j,k}^{N,S}$. To this end, we proceed similarly to [9, §2.2.1] by setting the slopes

134

$$(3.9) \quad ((b_1)_x)_{j,k} = \sigma_{j,k} \bar{A}_{j,k} \quad \text{and} \quad ((b_2)_y)_{j,k} = \sigma_{j,k} \bar{B}_{j,k},$$

135 where

136 (3.10) $\sigma_{j,k} = \min \{1, \sigma_{j,k}^x, \sigma_{j,k}^y\},$

137 and the scaling factors $\sigma_{j,k}^x$ and $\sigma_{j,k}^y$ are computed by

138 (3.11) $\sigma_{j,k}^x := \begin{cases} \min \{1, \sigma_{j,k}^{x,1}, \sigma_{j,k}^{x,2}\} & \text{if } \sigma_{j,k}^{x,1} > 0, \sigma_{j,k}^{x,2} > 0, \text{ and } \bar{A}_{j,k} \neq 0 \\ 0 & \text{otherwise} \end{cases}$

139 and

140 (3.12) $\sigma_{j,k}^y := \begin{cases} \min \{1, \sigma_{j,k}^{y,1}, \sigma_{j,k}^{y,2}\} & \text{if } \sigma_{j,k}^{y,1} > 0, \sigma_{j,k}^{y,2} > 0, \text{ and } \bar{B}_{j,k} \neq 0 \\ 0 & \text{otherwise,} \end{cases}$

141 where

142 (3.13)
$$\begin{aligned} \sigma_{j,k}^{x,1} &= \frac{2((\hat{b}_1)_{j,k}^E - (\bar{b}_1)_{j,k})}{\Delta x \bar{A}_{j,k}}, & \sigma_{j,k}^{x,2} &= \frac{2((\bar{b}_1)_{j,k} - (\hat{b}_1)_{j,k}^W)}{\Delta x \bar{A}_{j,k}}, \\ \sigma_{j,k}^{y,1} &= \frac{2((\hat{b}_2)_{j,k}^N - (\bar{b}_2)_{j,k})}{\Delta y \bar{B}_{j,k}}, & \sigma_{j,k}^{y,2} &= \frac{2((\bar{b}_2)_{j,k} - (\hat{b}_2)_{j,k}^S)}{\Delta y \bar{B}_{j,k}}, \end{aligned}$$

143 and $(\hat{b}_1)_{j,k}^{E,W}$ and $(\hat{b}_2)_{j,k}^{N,S}$ denote the point values of b_1 and b_2 , which have been reconstructed as described
144 above. We then correct the corresponding one-sided point values:

145 (3.14)
$$\begin{aligned} ((b_1)_{j,k})^E &= (\bar{b}_1)_{j,k} + \frac{\Delta x}{2}((b_1)_x)_{j,k}, & ((b_1)_{j+1,k})^W &= (\bar{b}_1)_{j+1,k} - \frac{\Delta x}{2}((b_1)_x)_{j+1,k}, \\ ((b_2)_{j,k})^N &= (\bar{b}_2)_{j,k} + \frac{\Delta y}{2}((b_2)_y)_{j,k}, & ((b_2)_{j,k+1})^S &= (\bar{b}_2)_{j,k+1} - \frac{\Delta y}{2}((b_2)_y)_{j,k+1}. \end{aligned}$$

146 • The one-sided point values $\tilde{U}_{j,k}^{E,W,N,S}$ are obtained by applying the generalized minmod reconstruction
147 directly to the A and B fields.

148 • The point values of the global variables \mathbf{I}^x and \mathbf{I}^y in (3.5) are computed recursively. We first set $\hat{x} = x_{\frac{1}{2}}$
149 and $\hat{y} = y_{\frac{1}{2}}$ so that $(\mathbf{I}^x)_{\frac{1}{2},k}^- := \mathbf{0}$ and $(\mathbf{I}^y)_{\frac{1}{2},k}^- := \mathbf{0}$, and then evaluate $(\mathbf{I}^x)_{\frac{1}{2},k}^+ = \mathbf{Q}_{\Psi,\frac{1}{2},k}^x$, $(\mathbf{I}^y)_{j,\frac{1}{2}}^+ = \mathbf{Q}_{\Psi,j,\frac{1}{2}}^y$,
150 and

151
$$\begin{aligned} (\mathbf{I}^x)_{j+\frac{1}{2},k}^- &= (\mathbf{I}^x)_{j-\frac{1}{2},k}^+ + \mathbf{Q}_{j,k}^x, & (\mathbf{I}^x)_{j+\frac{1}{2},k}^+ &= (\mathbf{I}^x)_{j+\frac{1}{2},k}^- + \mathbf{Q}_{\Psi,j+\frac{1}{2},k}^x, \\ (\mathbf{I}^y)_{j,k+\frac{1}{2}}^- &= (\mathbf{I}^y)_{j,k-\frac{1}{2}}^+ + \mathbf{Q}_{j,k}^y, & (\mathbf{I}^y)_{j,k+\frac{1}{2}}^+ &= (\mathbf{I}^y)_{j,k+\frac{1}{2}}^- + \mathbf{Q}_{\Psi,j,k+\frac{1}{2}}^y, \end{aligned}$$

152 for $j = 1, \dots, N_x$, $k = 1, \dots, N_y$. Here, $\mathbf{Q}_{j,k}^x$, $\mathbf{Q}_{\Psi,j+\frac{1}{2},k}^x$, $\mathbf{Q}_{j,k}^y$, and $\mathbf{Q}_{\Psi,j,k+\frac{1}{2}}^y$ are the terms reflecting the
153 contribution of the nonconservative terms $Q^x(\mathbf{U})\mathbf{U}_x$ and $Q^y(\mathbf{U})\mathbf{U}_y$. For the details on evaluating these
154 terms, we refer the readers to [9, §2.2.3].

• $P_{j+\frac{1}{2},k}^{\text{LCD}}$, $M_{j+\frac{1}{2},k}^{\text{LCD}}$, $Q_{j+\frac{1}{2},k}^{\text{LCD}}$, $P_{j,k+\frac{1}{2}}^{\text{LCD}}$, $M_{j,k+\frac{1}{2}}^{\text{LCD}}$, and $Q_{j,k+\frac{1}{2}}^{\text{LCD}}$ in (3.4) are diagonal matrices

$$\begin{aligned} P_{j+\frac{1}{2},k}^{\text{LCD}} &= \text{diag} \left((P_1^{\text{LCD}})_{j+\frac{1}{2},k}, \dots, (P_8^{\text{LCD}})_{j+\frac{1}{2},k} \right), & P_{j,k+\frac{1}{2}}^{\text{LCD}} &= \text{diag} \left((P_1^{\text{LCD}})_{j,k+\frac{1}{2}}, \dots, (P_8^{\text{LCD}})_{j,k+\frac{1}{2}} \right), \\ M_{j+\frac{1}{2},k}^{\text{LCD}} &= \text{diag} \left((M_1^{\text{LCD}})_{j+\frac{1}{2},k}, \dots, (M_8^{\text{LCD}})_{j+\frac{1}{2},k} \right), & M_{j,k+\frac{1}{2}}^{\text{LCD}} &= \text{diag} \left((M_1^{\text{LCD}})_{j,k+\frac{1}{2}}, \dots, (M_8^{\text{LCD}})_{j,k+\frac{1}{2}} \right), \\ Q_{j+\frac{1}{2},k}^{\text{LCD}} &= \text{diag} \left((Q_1^{\text{LCD}})_{j+\frac{1}{2},k}, \dots, (Q_8^{\text{LCD}})_{j+\frac{1}{2},k} \right), & Q_{j,k+\frac{1}{2}}^{\text{LCD}} &= \text{diag} \left((Q_1^{\text{LCD}})_{j,k+\frac{1}{2}}, \dots, (Q_8^{\text{LCD}})_{j,k+\frac{1}{2}} \right), \end{aligned}$$

where

$$\begin{aligned} ((P_i^{\text{LCD}})_{j+\frac{1}{2},k}, (M_i^{\text{LCD}})_{j+\frac{1}{2},k}, (Q_i^{\text{LCD}})_{j+\frac{1}{2},k}) &= \frac{((\lambda_i^+)_{j+\frac{1}{2},k}, -(\lambda_i^-)_{j+\frac{1}{2},k}, (\lambda_i^+)_{j+\frac{1}{2},k}(\lambda_i^-)_{j+\frac{1}{2},k})}{(\lambda_i^+)_{j+\frac{1}{2},k} - (\lambda_i^-)_{j+\frac{1}{2},k}}, \\ ((P_i^{\text{LCD}})_{j,k+\frac{1}{2}}, (M_i^{\text{LCD}})_{j,k+\frac{1}{2}}, (Q_i^{\text{LCD}})_{j,k+\frac{1}{2}}) &= \frac{((\lambda_i^+)_{j,k+\frac{1}{2}}, -(\lambda_i^-)_{j,k+\frac{1}{2}}, (\lambda_i^+)_{j,k+\frac{1}{2}}(\lambda_i^-)_{j,k+\frac{1}{2}})}{(\lambda_i^+)_{j,k+\frac{1}{2}} - (\lambda_i^-)_{j,k+\frac{1}{2}}}, \end{aligned}$$

155 with

$$\begin{aligned}
 156 \quad (3.15) \quad & (\lambda_i^+)_j + \frac{1}{2}, k = \max \{ \lambda_i(C^x(\mathbf{U}_{j,k}^E)), \lambda_i(C^x(\mathbf{U}_{j+1,k}^W)), \varepsilon \}, \\
 & (\lambda_i^-)_j + \frac{1}{2}, k = \min \{ \lambda_i(C^x(\mathbf{U}_{j,k}^E)), \lambda_i(C^x(\mathbf{U}_{j+1,k}^W)), -\varepsilon \}, \\
 & (\lambda_i^+)_j, k + \frac{1}{2} = \max \{ \lambda_i(C^y(\mathbf{U}_{j,k}^N)), \lambda_i(C^y(\mathbf{U}_{j,k+1}^S)), \varepsilon \}, \\
 & (\lambda_i^-)_j, k + \frac{1}{2} = \min \{ \lambda_i(C^y(\mathbf{U}_{j,k}^N)), \lambda_i(C^y(\mathbf{U}_{j,k+1}^S)), -\varepsilon \},
 \end{aligned}$$

157 and $\lambda_i(C^x(\mathbf{U}))$ and $\lambda_i(C^y(\mathbf{U}))$ are eigenvalues of C^x and C^y , $i = 1, \dots, 8$, respectively; see Appendix
158 A for details. In (3.15), ε is a small desingularization constant, which is taken to be 10^{-8} in all of the
159 numerical examples reported in §4.

- 160 • $R_{j+\frac{1}{2},k}^x$ and $R_{j,k+\frac{1}{2}}^y$ are the matrices of right eigenvectors of $\widehat{C}_{j+\frac{1}{2},k}^x = C^x(\widehat{\mathbf{U}}_{j+\frac{1}{2},k})$ and $\widehat{C}_{j,k+\frac{1}{2}}^y =$
161 $C^y(\widehat{\mathbf{U}}_{j,k+\frac{1}{2}})$, respectively. Here, we take $\widehat{\mathbf{U}}_{j+\frac{1}{2},k} = (\overline{\mathbf{U}}_{j,k} + \overline{\mathbf{U}}_{j+1,k})/2$ and $\widehat{\mathbf{U}}_{j,k+\frac{1}{2}} = (\overline{\mathbf{U}}_{j,k} + \overline{\mathbf{U}}_{j,k+1})/2$.
162 • $s_{j+\frac{1}{2},k}^\pm$ and $s_{j,k+\frac{1}{2}}^\pm$ are one-sided local speeds of propagation in the x - and y -direction, respectively. They
163 are estimated as in [9, §2.2.2].

164 *Remark 3.1.* We stress that the correction of the point values (3.9)–(3.14) together with the result
165 proven in [9, Theorem 2.2] enforce the local divergence-free condition (3.8).

166 **4. Numerical Examples.** In this section, we test the developed LCD-PCCU scheme on a number
167 of numerical examples and compare the obtained results with those computed by the PCCU scheme
168 from [9]. We numerically integrate the ODE systems (3.2) by the three-stage third-order strong stability
169 preserving (SSP) Runge-Kutta method (see, e.g., [21, 22]), use the CFL number 0.25, and set the minmod
170 parameter $\theta = 1.3$ (except for Example 5, where we take $\theta = 1$ to reduce oscillations). The specific heat
171 ratio γ is either 2 (Example 1), 5/3 (Examples 2–4), or 1.4 (Example 5).

172 In Examples 2 and 3, we will demonstrate how the discrete divergence $(\nabla \cdot \mathbf{b})_{j,k}$, defined in (3.8),
173 increases in time if the correction (3.9)–(3.13) of the slopes $((b_1)_x)_{j,k}$ and $((b_2)_y)_{j,k}$ is not implemented
174 (the corresponding scheme will be referred to as Uncorrected LCD-PCCU scheme).

175 **Example 1—Brio-Wu Shock-Tube Problem.** In the first example taken from [5], we consider
176 the one-dimensional (1-D) Riemann problem, which is a benchmark widely used to test the ability of
177 schemes to capture compound waves that emerge out of the initial data,

$$178 \quad (\rho, u, v, w, b1, b2, b3, p)(x, 0) = \begin{cases} (1, 0, 0, 0, 0.75, 1, 0, 1) & \text{if } x < 0, \\ (0.125, 0, 0, 0, 0.75, -1, 0, 0.1) & \text{otherwise,} \end{cases}$$

179 which depend on x only. We conduct a 2-D computation on the domain $[-1, 1] \times [-0.01, 0.01]$ subject to
180 the free boundary conditions.

181 We compute the solutions by the LCD-PCCU and PCCU schemes until the final time $t = 0.2$ on a
182 uniform mesh consisting of 200×2 cells. The cross-sectional profiles at $y = 0$ of ρ , b_1 , and b_2 are presented
183 in Figure 4.1 along with the reference solution computed by the PCCU scheme on a significantly finer mesh
184 of 10000×2 cells. One can observe that the solution consists of several nonsmooth structures, including
185 rarefaction waves, shock waves traveling at various speeds, a contact discontinuity, and a compound shock
186 wave. Both the LCD-PCCU and PCCU schemes successfully capture all of these complex structures.
187 However, the numerical results obtained by the LCD-PCCU scheme exhibit somewhat higher resolution
188 compared to those produced by the PCCU scheme.

Example 2—Circularly Polarized Alfvén Wave. In the second example taken from [36], we
consider the time evolution of a circularly polarized Alfvén wave that travels at a constant speed at an
angle of $\alpha = \pi/6$ with respect to the x -axis. In this example, designed to check the experimental order of
accuracy of the studied schemes, the initial conditions are

$$\begin{aligned}
 \rho(x, y, 0) &\equiv 1, & u(x, y, 0) &= v_\parallel \cos \alpha + v_\perp \sin \alpha, & v(x, y, 0) &= v_\parallel \sin \alpha - v_\perp \cos \alpha, \\
 p(x, y, 0) &\equiv 0.1, & b_1(x, y, 0) &= b_\parallel \cos \alpha + b_\perp \sin \alpha, & b_2(x, y, 0) &= b_\parallel \sin \alpha - b_\perp \cos \alpha, \\
 w(x, y, 0) &= b_3(x, y, 0) = 0.1 \cos [2\pi(x \cos \alpha + y \sin \alpha)],
 \end{aligned}$$

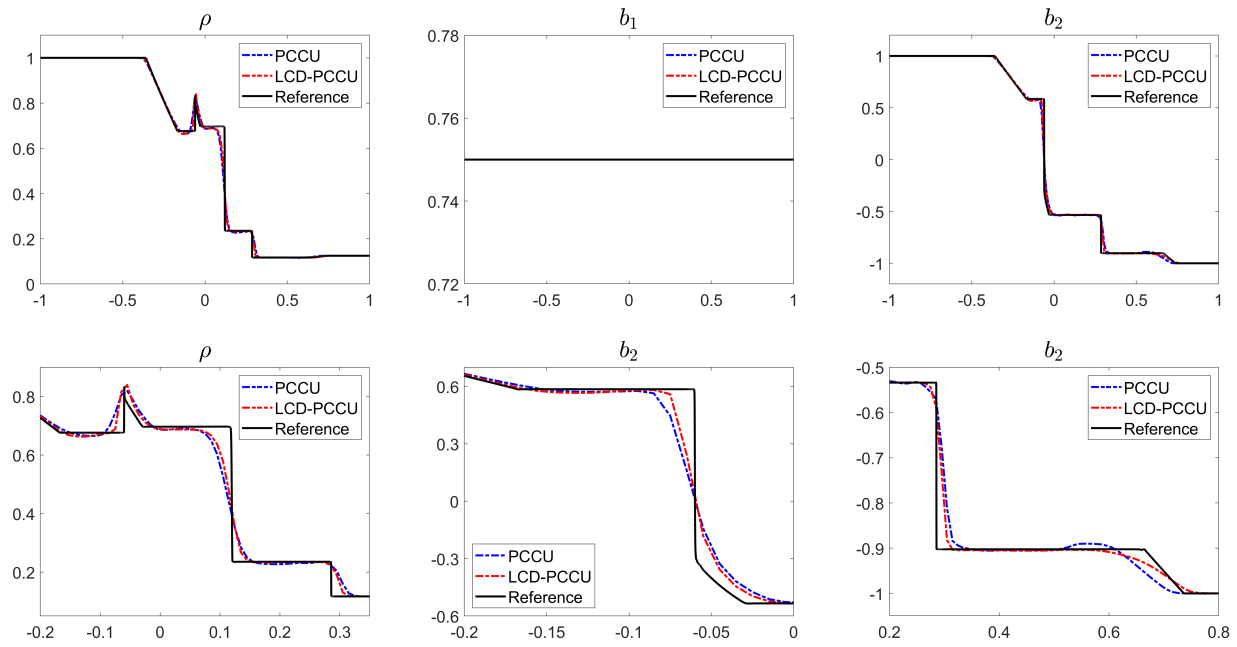


FIG. 4.1. Example 1: ρ , b_1 , and b_2 computed by the LCD-PCCU and PCCU schemes (top row) and zooms for ρ and b_2 at $x \in [-0.2, 0.35]$, $[-0.2, 0]$, and $[0.2, 0.8]$ (bottom row).

where

$$v_{\parallel} = 0, \quad b_{\parallel} = 1, \quad v_{\perp} = b_{\perp} = 0.1 \sin [2\pi(x \cos \alpha + y \sin \alpha)],$$

and the periodic boundary conditions are imposed in the computational domain $[0, \frac{1}{\cos \alpha}] \times [0, \frac{1}{\sin \alpha}]$. It is easy to show that the solution of the resulting initial-boundary value problem is a traveling wave, which returns to its initial position at any integer time t .

We compute the solutions by the LCD-PCCU and PCCU schemes until the final time $t = 5$ on a sequence of uniform meshes with 20×20 , 40×40 , 80×80 , 160×160 , and 320×320 cells, and compute the L^1 -norm of the differences between the numerical and exact solutions. We report the L^1 -errors and corresponding experimental rates of convergence for both u and b_3 in Table 4.1, where one can see that while both the LCD-PCCU and PCCU schemes achieve the expected second order of accuracy, the magnitudes of the errors are slightly smaller for the proposed LCD-PCCU scheme.

TABLE 4.1
Example 2: L^1 -errors and experimental convergence rates for u and b_3 computed by the LCD-PCCU and PCCU schemes.

Mesh	LCD-PCCU Scheme				PCCU Scheme			
	u		b_3		u		b_3	
	Error	Rate	Error	Rate	Error	Rate	Error	Rate
20×20	2.69e-2	—	4.50e-2	—	3.38e-2	—	6.45e-2	—
40×40	7.83e-3	1.78	1.18e-2	1.93	7.98e-3	2.08	1.67e-2	1.95
80×80	2.29e-3	1.78	3.29e-3	1.84	2.46e-3	1.70	5.32e-3	1.65
160×160	5.75e-4	1.99	8.31e-4	1.98	6.48e-4	1.93	1.41e-3	1.92
320×320	1.34e-4	2.10	2.19e-4	1.93	1.54e-4	2.08	3.34e-4	2.07

Figure 4.2 presents the time evolution of the L^1 - and L^∞ -norms of $(\nabla \cdot \mathbf{b})_{j,k}$ computed by the Uncorrected LCD-PCCU scheme on a uniform 320×320 mesh. As one can see, the magnitudes of both norms are comparable or even exceed the size of the formal truncation error, which is about 10^{-5} on this grid. This suggests that the use of the Uncorrected LCD-PCCU scheme may lead to a substantial

202 numerical inaccuracy, and thus applying the divergence-free correction might be essential for ensuring the physical consistency and long-term stability of the simulation.

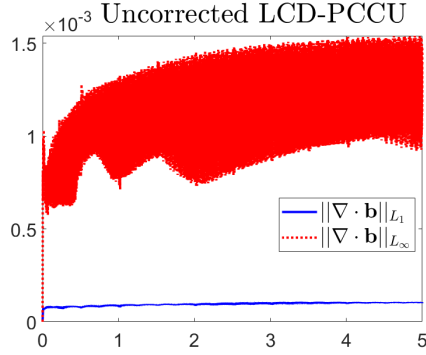


FIG. 4.2. Example 2: Time evolution of the L^1 - and L^∞ -norms of $(\nabla \cdot \mathbf{b})_{j,k}$ computed by the Uncorrected LCD-PCCU scheme on a uniform 320×320 mesh.

203

Example 3—Orszag-Tang Vortex Problem. In this example taken from [30], we consider the Orszag-Tang vortex problem, which has been widely used as a benchmark due to the formation and interaction of multiple shocks as the system evolves in time and to the presence of many important features of MHD turbulence. The initial conditions,

$$\begin{aligned}\rho(x, y, 0) &\equiv \gamma^2, & u(x, y, 0) &= -\sin y, & v(x, y, 0) &= \sin x, & w(x, y, 0) &\equiv 0, \\ b_1(x, y, 0) &= -\sin y, & b_2(x, y, 0) &= \sin(2x), & b_3(x, y, 0) &\equiv 0, & p(x, y, 0) &\equiv \gamma,\end{aligned}$$

204 are prescribed in the computational domain $[0, 2\pi] \times [0, 2\pi]$ subject to the periodic boundary conditions.

205 We compute the numerical solutions by both the LCD-PCCU and PCCU schemes until the final time
206 $t = 4$ using a uniform 200×200 mesh and plot the obtained densities in Figure 4.3. As one can see, the
207 LCD-PCCU solution is sharper, and this can be further seen in Figure 4.4, where we plot the 1-D slices
208 of both densities along $y = \pi$ together with the reference solution computed by the PCCU scheme on
1000 \times 1000 uniform mesh.

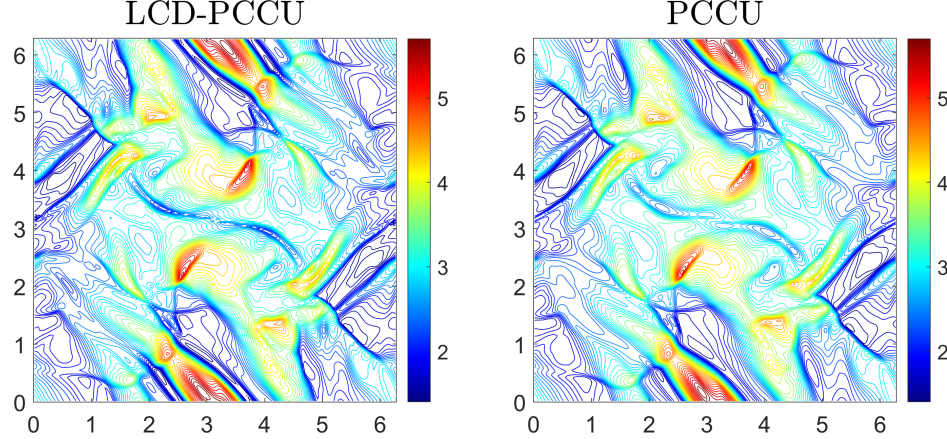


FIG. 4.3. Example 3: Density ρ computed by the LCD-PCCU (left) and PCCU (right) schemes.

209

210 The time evolution of the L^1 - and L^∞ -norms of $(\nabla \cdot \mathbf{b})_{j,k}$ computed by the Uncorrected LCD-PCCU
211 scheme is presented in Figure 4.5. As one can see, the magnitudes of both norms increase in time and
212 in this example, they are several orders of magnitude larger than the formal truncation error, which is
213 about 10^{-3} on this grid. Consequently, applying the divergence-free correction is essential for ensuring
214 the physical consistency and long-term stability of the simulation.

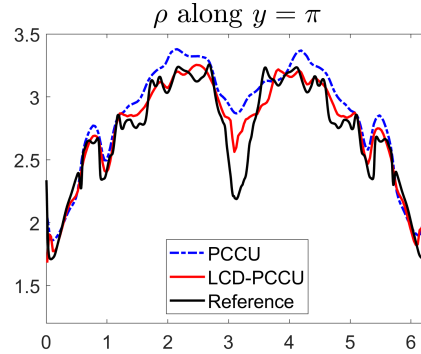


FIG. 4.4. Example 3: 1-D slices along the line $y = \pi$ of the solutions from Figure 4.3 together with the reference solution.

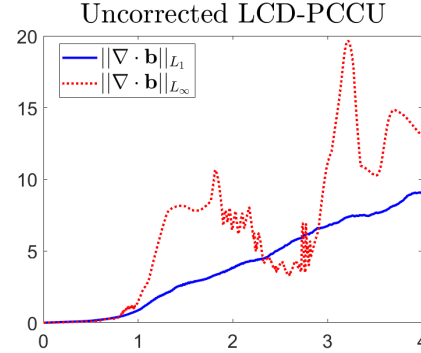


FIG. 4.5. Example 3: Time evolution of the L^1 - and L^∞ -norms of $(\nabla \cdot \mathbf{b})_{j,k}$ computed by the Uncorrected LCD-PCCU scheme.

215 **Example 4—Rotor Problem.** In this example, we study the “second rotor problem”, originally
216 introduced in [3,36] as a benchmark featuring a rapidly rotating, dense fluid disk embedded in a stationary
217 background. As time progresses, the disk undergoes both expansion and rotation.

218 The initial conditions are

$$219 \quad (\rho, u, v) \Big|_{(x,y,0)} = \begin{cases} \left(10, \frac{0.5 - y}{r_0}, \frac{x - 0.5}{r_0} \right), & r < 0.1, \\ \left(1 + 9\mu, \frac{\mu(0.5 - y)}{r}, \frac{\mu(x - 0.5)}{r} \right), & 0.1 \leq r \leq 0.115, \\ (1, 0, 0), & r > 0.115, \end{cases}$$

$$w(x, y, 0) = b_2(x, y, 0) = b_3(x, y, 0) \equiv 0, \quad b_1(x, y, 0) \equiv \frac{2.5}{\sqrt{4\pi}}, \quad p(x, y, 0) \equiv 0.5,$$

220 where $r = \sqrt{(x - 0.5)^2 + (y - 0.5)^2}$, $r_0 = 0.1$, and $\mu = (0.115 - r)/0.015$. We use the periodic boundary
221 conditions in the computational domain $[0, 1] \times [0, 1]$.

222 We compute the numerical solutions by both the LCD-PCCU and PCCU schemes until the final time
223 $t = 0.295$ using a uniform 200×200 mesh and plot the obtained ρ and p in Figure 4.6, where one can see
224 that the LCD-PCCU scheme achieves higher resolution. To further demonstrate this, we show (in Figure
225 4.7) the 1-D slices of both densities along $x = 0.3$ together with the reference solution computed by the
226 PCCU scheme on 1000×1000 uniform mesh.

227 **Example 5—Blast Problem.** In the last example taken from [3], we consider the blast problem,
228 which poses a significant challenge due to the low gas pressure and presence of strong magnetosonic shocks,
229 which frequently lead to the occurrence of negative pressures near the shocks; see [26,27] and references
230 therein.

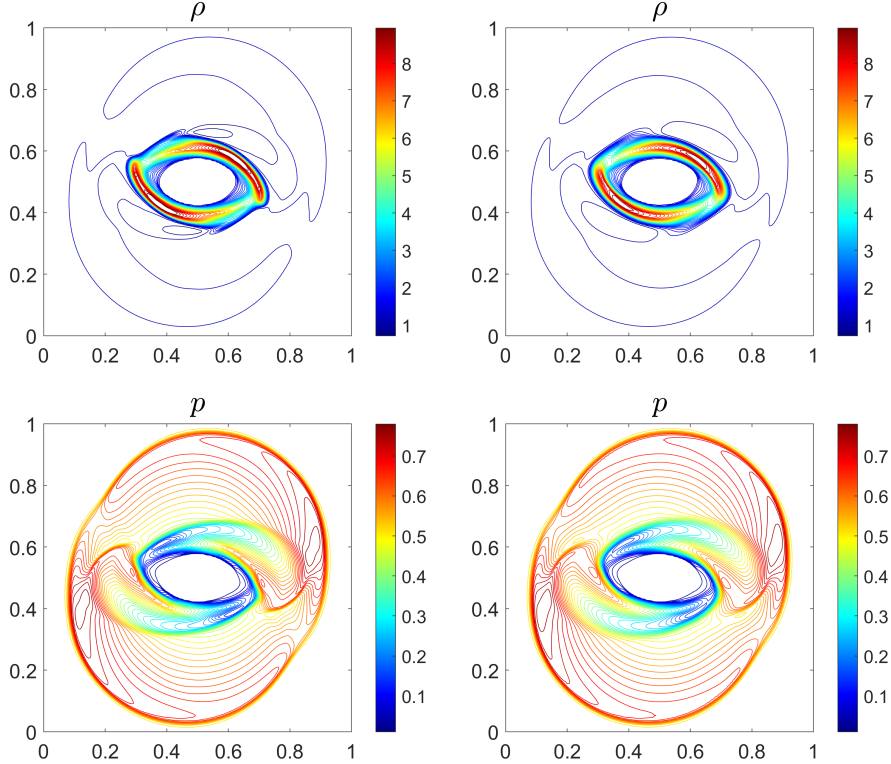


FIG. 4.6. Example 4: Density ρ (top row) and pressure p (bottom row) computed by the LCD-PCCU (left column) and PCCU (right column) schemes.

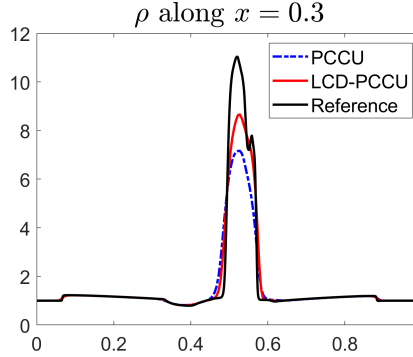


FIG. 4.7. Example 4: 1-D slices along the line $x = 0.3$ of the densities from Figure 4.6 together with the reference solution.

The initial conditions,

$$(\rho, u, v, w, b_1, b_2, b_3) \Big|_{(x,y,0)} = \left(1, 0, 0, 0, \frac{50}{\sqrt{\pi}}, 0, 0 \right), \quad p(x, y, 0) = \begin{cases} 1000, & \sqrt{x^2 + y^2} < 0.1, \\ 0.1 & \text{otherwise,} \end{cases}$$

are prescribed in the computational domain $[-0.5, 0.5] \times [-0.5, 0.5]$ subject to the zero-order extrapolation imposed at the boundary.

We compute the numerical solutions by both the LCD-PCCU and PCCU schemes until the final time $t = 0.01$ on a uniform 200×200 mesh and plot the obtained density ρ , pressure p , velocity magnitude $|\mathbf{u}|$, and magnetic pressure $|\mathbf{b}|^2/2$ in Figure 4.8. As one can see, the numerical results computed by the LCD-PCCU scheme are visibly sharper. However, they contain wiggles in the areas of high density and pressure. To experimentally verify that these structures are not numerical artifacts, we refine the mesh and perform the same computations on a uniform 1000×1000 mesh. The obtained results reported in the

left two columns of Figure 4.9, indicate that similar structures start developing in the PCCU solution as well. We thus further refine the mesh and run the PCCU simulation on an even finer 2000×2000 mesh; see Figure 4.9 (right column). One can observe that those wiggly structures are now clearly present in the PCCU results. One can notice that the resolution achieved by the LCD-PCCU scheme on the 1000×1000 mesh is practically the same as that achieved by the PCCU scheme on the 2000×2000 mesh. This clearly indicates an advantage of the proposed LCD-PCCU scheme.

5. Conclusions. In this paper, we have developed a locally divergence-free local characteristic decomposition (LCD) based path-conservative central-upwind (LCD-PCCU) scheme for the ideal magnetohydrodynamics (MHD) equations. The proposed scheme is applied to the Godunov-Powell nonconservative modifications of the studied MHD systems, which have a complete eigenstructure required to derive LCD-based central-upwind numerical fluxes; see [8, 12]. In order to ensure the local divergence-free property, we have followed [9] and augmented the studied systems with the evolution equations for the corresponding derivatives of the magnetic field components and by using these evolved quantities in the design of a special piecewise linear reconstruction of the magnetic field, which also guarantees a non-oscillatory nature of the resulting scheme. The designed LCD-PCCU scheme has been tested on several benchmarks, and the obtained numerical results demonstrate that the proposed scheme outperforms its PCCU counterpart from [9].

Appendix A. Eigendecomposition for Conservative Variables. In this appendix, we provide the reader with the matrices used in the LCD of the quasi-linear system (2.9); see [5] for details.

First, the matrices C^x and C^y are

$$(A.1) \quad C^x(\mathbf{U}) = \begin{pmatrix} 0 & 1 & 0 & 0 & 0 & 0 & 0 & 0 \\ a_1 & \gamma_3 u_N & \gamma_1 u_T & \gamma_1 w & -\gamma_1 & b_1 & \gamma_2 b_2 & \gamma_2 b_3 \\ -u_N u_T & u_T & u_N & 0 & 0 & b_2 & -b_N & 0 \\ -u_N w & w & 0 & u_N & 0 & b_3 & 0 & -b_N \\ a_2 & a_3 & a_4 & a_5 & \gamma u_N & \mathbf{u} \cdot \mathbf{b} & a_6 & a_7 \\ 0 & 0 & 0 & 0 & 0 & u & 0 & 0 \\ \frac{u_T b_N - u_N b_T}{\rho} & \frac{b_T}{\rho} & -\frac{b_N}{\rho} & 0 & 0 & v & u_N & 0 \\ \frac{w b_N - u_N b_3}{\rho} & \frac{b_3}{\rho} & 0 & -\frac{b_N}{\rho} & 0 & w & 0 & u_N \end{pmatrix},$$

and

$$(A.2) \quad C^y(\mathbf{U}) = \begin{pmatrix} 0 & 0 & 1 & 0 & 0 & 0 & 0 & 0 \\ -u_N u_T & u_N & u_T & 0 & 0 & -b_N & b_1 & 0 \\ a_1 & \gamma_1 u_T & \gamma_3 u_N & \gamma_1 w & -\gamma_1 & \gamma_2 b_2 & b_2 & \gamma_2 b_3 \\ -u_N w & 0 & w & u_N & 0 & 0 & b_3 & -b_N \\ a_2 & a_4 & a_3 & a_5 & \gamma u_N & a_6 & \mathbf{u} \cdot \mathbf{b} & a_7 \\ \frac{u_T b_N - u_N b_T}{\rho} & -\frac{b_N}{\rho} & \frac{b_T}{\rho} & 0 & 0 & u_N & u & 0 \\ 0 & 0 & 0 & 0 & 0 & 0 & v & 0 \\ \frac{w b_N - u_N b_3}{\rho} & 0 & \frac{b_3}{\rho} & -\frac{b_N}{\rho} & 0 & 0 & w & u_N \end{pmatrix},$$

where u_N , b_N and u_T , b_T are the normal and tangential components of \mathbf{u} and \mathbf{b} with respect to the x - and y -axis, namely,

$$(u_N, u_T, b_N, b_T) := \begin{cases} (u, v, b_1, b_2) & \text{in the } x\text{-direction (in (A.1)),} \\ (v, u, b_2, b_1) & \text{in the } y\text{-direction (in (A.2)),} \end{cases}$$

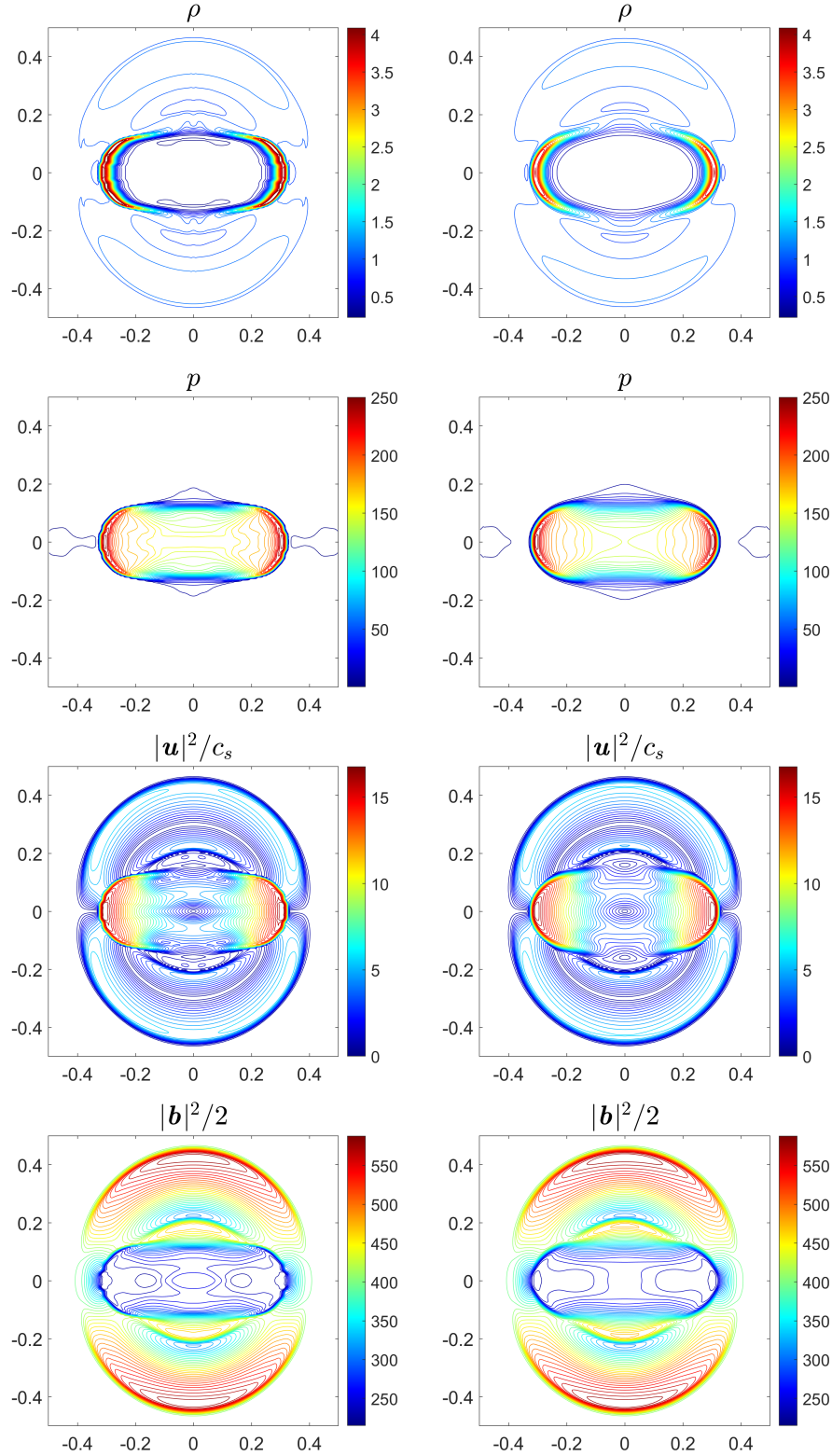


FIG. 4.8. Example 5: Density ρ (top row), pressure p (second row), velocity magnitude $|\mathbf{u}|$ (third row), and magnetic pressure $|\mathbf{b}|^2/2$ (bottom row) computed by the LCD-PCCU (left column) and PCCU (right column) schemes on a uniform 200×200 mesh.

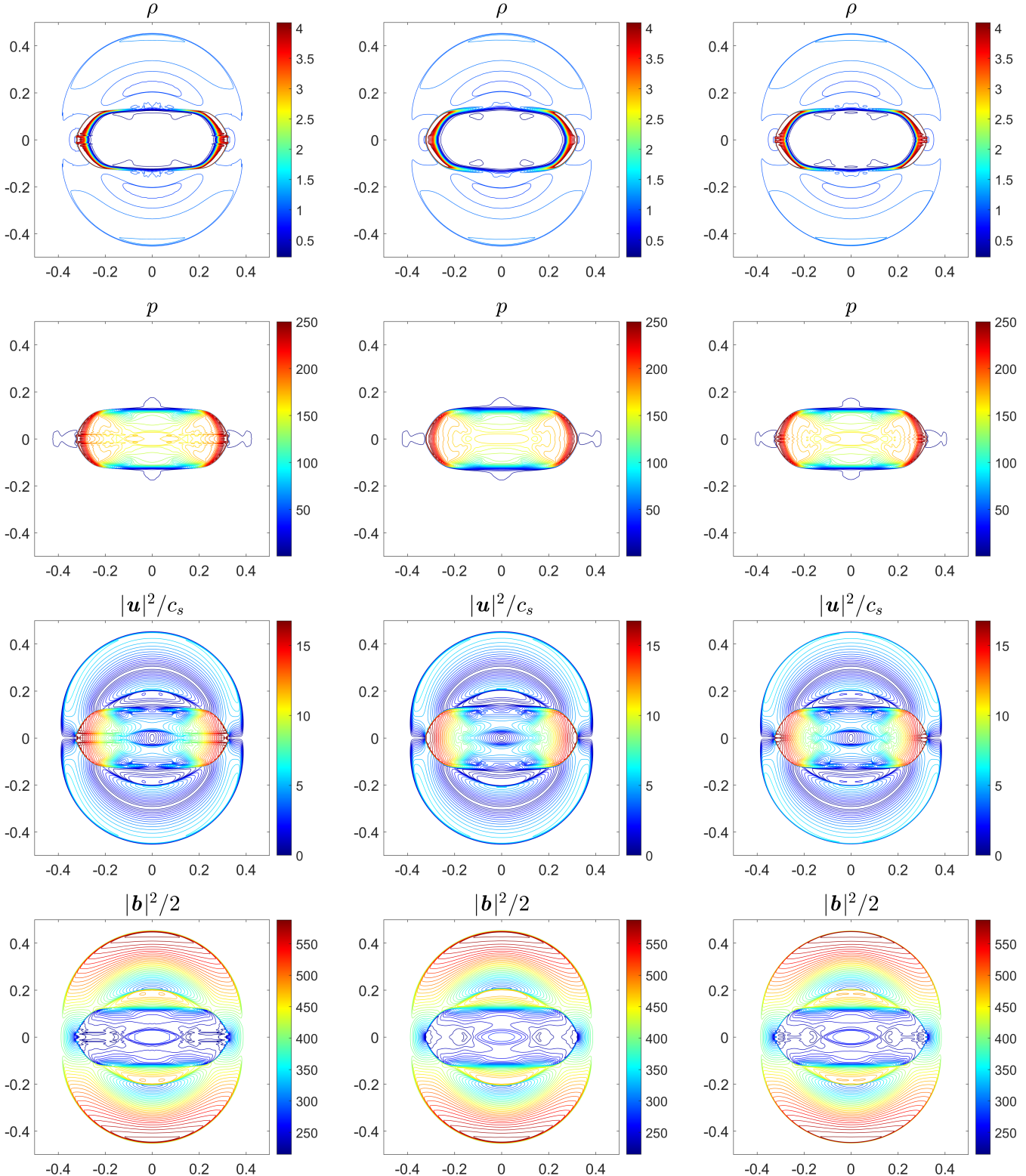


FIG. 4.9. Example 5: Density ρ (top row), pressure p (second row), velocity magnitude $|u|$ (third row), and magnetic pressure $|b|^2/2$ (bottom row) computed by the LCD-PCCU scheme on a uniform 1000×1000 mesh (left column) and PCCU scheme on uniform 1000×1000 (middle column) and 2000×2000 (right column) meshes.

$\gamma_n := n - \gamma$ for $n = 1, 2, 3$, and

$$\begin{aligned} a_1 &:= -\frac{\gamma_3}{2}u_N^2 - \frac{\gamma_1}{2}(u_T^2 + w^2), & a_2 &:= u_N \left(\frac{\gamma_1}{2\rho} \left(\mathcal{E} + p + \frac{1}{2}|\mathbf{b}|^2 \right) |\mathbf{u}|^2 - \frac{b_N}{\rho}(\mathbf{u} \cdot \mathbf{b}) \right), \\ a_3 &:= \frac{1}{\rho} \left(\mathcal{E} + p + \frac{1}{2}|\mathbf{b}|^2 \right) - \frac{b_N^2}{\rho} + \gamma_1 u_N^2, & a_4 &:= \gamma_1 u_N u_T - \frac{1}{\rho} b_N b_T, & a_5 &:= \gamma_1 u_N w - \frac{1}{\rho} b_N b_3, \\ a_6 &:= \gamma_2 u_N b_T - u_T b_N, & a_7 &:= \gamma_2 u_N b_3 - w b_N. \end{aligned}$$

One can show that the eigenvalues of both C^x and C^y are given by

$$(A.3) \quad \lambda_{1,8} = u_N \mp c_f, \quad \lambda_{2,7} = u_N \mp c_a, \quad \lambda_{3,6} = u_N \mp c_s, \quad \lambda_4 = \lambda_5 = u_N,$$

where

$$(A.4) \quad c_a = \sqrt{\frac{b_N^2}{\rho}}, \quad c_{f,s} = \left[\frac{1}{2} \left(c^2 + \frac{|\mathbf{b}|^2}{\rho} \pm \sqrt{\left(c^2 + \frac{|\mathbf{b}|^2}{\rho} \right)^2 - 4c^2 \frac{b_N^2}{\rho}} \right) \right]^{\frac{1}{2}},$$

and $c := \sqrt{\gamma p / \rho}$ is the speed of sound.

Finally, we provide the formula for the matrices R^x and R^y , which diagonalize C^x and C^y , that is, $(R^x)^{-1}C^xR^x$ and $(R^y)^{-1}C^yR^y$ are diagonal. One can show that $R^x = [\mathbf{r}_1^x | \mathbf{r}_2^x | \dots | \mathbf{r}_7^x | \mathbf{r}_8^x]$ and $(R^x)^{-1} = [\ell_1^x | \ell_2^x | \dots | \ell_7^x | \ell_8^x]^\top$, where \mathbf{r}_i^x and ℓ_i^x , $i = 1, \dots, 8$ are the right and left eigenvectors of C^x :

$$\begin{aligned} 270 \quad \mathbf{r}_{1,8}^x &= \begin{pmatrix} \alpha_f \\ \alpha_f(u_N \mp c_f) \\ \alpha_f u_T \pm \alpha_s \beta_1 \beta_2 c_a \\ \alpha_f w \pm \alpha_s \beta_1 \beta_3 c_a \\ \frac{1}{2} \alpha_f |\mathbf{u}|^2 + \mu_f^\mp \\ 0 \\ \frac{1}{\sqrt{\rho}} \alpha_s \beta_2 c_f \\ \frac{1}{\sqrt{\rho}} \alpha_s \beta_3 c_f \end{pmatrix}, \quad \mathbf{r}_{2,7}^x = \begin{pmatrix} 0 \\ 0 \\ \pm \beta_1 \beta_3 \\ \mp \beta_1 \beta_2 \\ \pm (\beta_3 u_T - \beta_2 w) \beta_1 \\ 0 \\ \frac{1}{\sqrt{\rho}} \beta_3 \\ -\frac{1}{\sqrt{\rho}} \beta_2 \end{pmatrix}, \quad \mathbf{r}_{3,6}^x = \begin{pmatrix} \alpha_s \\ \alpha_s(u_N \mp c_s) \\ \alpha_s u_T \mp \alpha_f \beta_1 \beta_2 c \\ \alpha_s w \mp \alpha_f \beta_1 \beta_3 c \\ \frac{1}{2} \alpha_s |\mathbf{u}|^2 + \mu_s^\mp \\ 0 \\ -\frac{1}{c_f \sqrt{\rho}} \alpha_f \beta_2 c^2 \\ -\frac{1}{c_f \sqrt{\rho}} \alpha_f \beta_3 c^2 \end{pmatrix}, \\ 271 \quad \mathbf{r}_4^x &= \left(1, u_N, u_T, w, \frac{1}{2} |\mathbf{u}|^2, 0, 0, 0 \right)^\top, \quad \mathbf{r}_5^x = (0, 0, 0, 0, 0, 1, 0, 0)^\top, \quad \ell_5^x = (0, 0, 0, 0, 0, 1, 0, 0)^\top, \\ 272 \quad \ell_{1,8}^x &= \begin{pmatrix} \frac{1}{2} \theta_1 \alpha_f c^2 |\mathbf{u}|^2 \pm \theta_2 [\alpha_f c u_N \beta_1 - \alpha_s c_s (\beta_2 u_T + \beta_3 w)] \\ -\theta_1 \alpha_f c^2 u_N \mp \theta_2 \alpha_f c \beta_1 \\ -\theta_1 \alpha_f c^2 u_T \pm \theta_2 \alpha_s c_s \beta_2 \\ -\theta_1 \alpha_f c^2 w \pm \theta_2 \alpha_s c_s \beta_3 \\ \theta_1 \alpha_f c^2 \\ 0 \\ \theta_1 \sqrt{\rho} \alpha_s \beta_2 c_f \left(c_s^2 - \frac{\gamma_2}{\gamma_1} c^2 \right) \\ \theta_1 \sqrt{\rho} \alpha_s \beta_3 c_f \left(c_s^2 - \frac{\gamma_2}{\gamma_1} c^2 \right) \end{pmatrix}, \quad \ell_{2,7}^x = \begin{pmatrix} \mp \frac{1}{2} \beta_1 (\beta_3 u_T - \beta_2 w) \\ 0 \\ \pm \frac{1}{2} \beta_1 \beta_3 \\ \mp \frac{1}{2} \beta_1 \beta_2 \\ 0 \\ 0 \\ \frac{1}{2} \sqrt{\rho} \beta_3 \\ -\frac{1}{2} \sqrt{\rho} \beta_2 \end{pmatrix}, \end{aligned}$$

$$273 \quad \ell_{3,6}^x = \begin{pmatrix} \frac{1}{2}\theta_1\alpha_s c_f^2 |\mathbf{u}|^2 \pm \theta_2 [\alpha_s c_a u_N \beta_1 + \alpha_f c_f (\beta_2 u_T + \beta_3 w)] \\ -\theta_1\alpha_s c_f^2 u_N \mp \theta_2\alpha_s c_a \beta_1 \\ -\theta_1\alpha_s c_f^2 u_T \mp \theta_2\alpha_f c_f \beta_2 \\ -\theta_1\alpha_s c_f^2 w \mp \theta_2\alpha_f c_f \beta_3 \\ \theta_1\alpha_s c_f^2 \\ 0 \\ -\theta_1\sqrt{\rho}\alpha_f \beta_2 c_f \left(c_f^2 - \frac{\gamma_2}{\gamma_1} c^2 \right) \\ -\theta_1\sqrt{\rho}\alpha_f \beta_3 c_f \left(c_f^2 - \frac{\gamma_2}{\gamma_1} c^2 \right) \end{pmatrix}, \quad \ell_4^x = \begin{pmatrix} 1 - \theta_1 \left(\alpha_f^2 c^2 + \alpha_s^2 c_f^2 \right) |\mathbf{u}|^2 \\ 2\theta_1 \left(\alpha_f^2 c^2 + \alpha_s^2 c_f^2 \right) u_N \\ 2\theta_1 \left(\alpha_f^2 c^2 + \alpha_s^2 c_f^2 \right) u_T \\ 2\theta_1 \left(\alpha_f^2 c^2 + \alpha_s^2 c_f^2 \right) w \\ -2\theta_1 \left(\alpha_f^2 c^2 + \alpha_s^2 c_f^2 \right) \\ 0 \\ 2\theta_1 \sqrt{\rho} \alpha_f \alpha_s \beta_2 c_f \left(c_f^2 - c_s^2 \right) \\ 2\theta_1 \sqrt{\rho} \alpha_f \alpha_s \beta_3 c_f \left(c_f^2 - c_s^2 \right) \end{pmatrix}.$$

Here,

$$\beta_1 := \text{sign}(b_N), \quad (\beta_2, \beta_3) := \begin{cases} \left(\frac{1}{\sqrt{2}}, \frac{1}{\sqrt{2}} \right), & \text{if } b_T = b_3 = 0, \\ \left(\frac{b_T}{\sqrt{b_T^2 + b_3^2}}, \frac{b_3}{\sqrt{b_T^2 + b_3^2}} \right) & \text{otherwise,} \end{cases}$$

$$(\alpha_f, \alpha_s) := \begin{cases} (1, 1) & \text{if } b_T = b_3 = 0, \\ \left(\sqrt{\frac{(c_f^2 - c_a^2)}{(c_f^2 - c_s^2)}}, \sqrt{\frac{(c_f^2 - c^2)}{(c_f^2 - c_s^2)}} \right) & \text{otherwise,} \end{cases}$$

$$\theta_1 := \frac{1}{2} \left[\alpha_f^2 c^2 \left(c_f^2 - \frac{\gamma_2}{\gamma_1} c^2 \right) + \alpha_s^2 c^2 \left(c_s^2 - \frac{\gamma_2}{\gamma_1} c^2 \right) \right]^{-1}, \quad \theta_2 := \frac{1}{2} \left[\alpha_f^2 c_f a \beta_1 + \alpha_s^2 c_s c_a \beta_1 \right]^{-1},$$

$$\mu_f^\mp := -\frac{\alpha_f c_f^2}{\gamma_1} \mp \alpha_f c_f u_N \pm \alpha_s c_a \beta_1 (\beta_2 u_T + \beta_3 w) + \frac{\gamma_2}{\gamma_1} \alpha_f (c_f^2 - c^2),$$

$$\mu_s^\mp := -\frac{\alpha_s c_s^2}{\gamma_1} \mp \alpha_s c_s u_N \mp \alpha_f c \beta_1 (\beta_2 u_T + \beta_3 w) + \frac{\gamma_2}{\gamma_1} \alpha_s (c_s^2 - c^2).$$

274 The structure of the matrices R^y and $(R^y)^{-1}$ is similar, but in all of the right and left eigenvectors
275 above, one needs to switch the second and third components as well as the sixth and seventh components.

276 **Appendix B. Eigendecomposition for Primitive Variables.** In this appendix, we provide the
277 reader with the matrices used in the LCD for the quasi-linear system (2.10); see [34] for details.

278 First, the matrices D^x and D^y are

$$279 \quad D^x(\mathbf{V}) = \begin{pmatrix} u & \rho & 0 & 0 & 0 & 0 & 0 & 0 \\ 0 & u & 0 & 0 & \frac{1}{\rho} & 0 & \frac{b_2}{\rho} & \frac{b_3}{\rho} \\ 0 & 0 & u & 0 & 0 & 0 & -\frac{b_1}{\rho} & 0 \\ 0 & 0 & 0 & u & 0 & 0 & 0 & -\frac{b_1}{\rho} \\ 0 & \gamma p & 0 & 0 & u & 0 & 0 & 0 \\ 0 & 0 & 0 & 0 & 0 & u & 0 & 0 \\ 0 & b_2 & -b_1 & 0 & 0 & 0 & u & 0 \\ 0 & b_3 & 0 & -b_1 & 0 & 0 & 0 & u \end{pmatrix}$$

280 and

$$281 \quad D^y(\mathbf{V}) = \begin{pmatrix} v & 0 & \rho & 0 & 0 & 0 & 0 & 0 \\ 0 & v & 0 & 0 & 0 & -\frac{b_2}{\rho} & 0 & 0 \\ 0 & 0 & v & 0 & \frac{1}{\rho} & \frac{b_1}{\rho} & 0 & \frac{b_3}{\rho} \\ 0 & 0 & 0 & v & 0 & 0 & 0 & -\frac{b_2}{\rho} \\ 0 & 0 & \gamma p & 0 & v & 0 & 0 & 0 \\ 0 & -b_2 & b_1 & 0 & 0 & v & 0 & 0 \\ 0 & 0 & 0 & 0 & 0 & 0 & v & 0 \\ 0 & 0 & b_3 & -b_2 & 0 & 0 & 0 & v \end{pmatrix}.$$

282 We note that the matrices D^x and D^y have the same eigenvalues (A.3)–(A.4) as the matrices C^x and
283 C^y , but different eigenvectors. The matrix T^x , which diagonalizes D^x is $T^x = [\mathbf{r}_1^x | \mathbf{r}_2^x | \dots | \mathbf{r}_7^x | \mathbf{r}_8^x]$ and its
284 inverse is $(T^x)^{-1} = [\ell_1^x | \ell_2^x | \dots | \ell_7^x | \ell_8^x]^\top$, where \mathbf{r}_i^x and ℓ_i^x , $i = 1, \dots, 8$ are the right and left eigenvectors
285 of D^x :

$$286 \quad \mathbf{r}_{1,8}^x = \begin{pmatrix} \hat{\alpha}_f \rho \\ \mp \hat{\alpha}_f c_f \\ \pm \hat{\alpha}_s c_s \beta_1 \beta_2 \\ \pm \hat{\alpha}_s c_s \beta_1 \beta_3 \\ \hat{\alpha}_f \rho c^2 \\ 0 \\ \hat{\alpha}_s \sqrt{\rho} c \beta_2 \\ \hat{\alpha}_s \sqrt{\rho} c \beta_3 \end{pmatrix}, \quad \mathbf{r}_{2,7}^x = \begin{pmatrix} 0 \\ 0 \\ \mp \beta_3 \\ \pm \beta_2 \\ 0 \\ 0 \\ -\sqrt{\rho} \beta_1 \beta_3 \\ \sqrt{\rho} \beta_1 \beta_2 \end{pmatrix}, \quad \mathbf{r}_{3,6}^x = \begin{pmatrix} \hat{\alpha}_s \rho \\ \mp \hat{\alpha}_s c_s \\ \mp \hat{\alpha}_f c_f \beta_1 \beta_2 \\ \mp \hat{\alpha}_f c_f \beta_1 \beta_3 \\ \hat{\alpha}_s \rho c^2 \\ 0 \\ -\hat{\alpha}_f \sqrt{\rho} a \beta_2 \\ -\hat{\alpha}_f \sqrt{\rho} a \beta_3 \end{pmatrix},$$

$$287 \quad \mathbf{r}_4^x = (1, 0, 0, 0, 0, 0, 0, 0)^\top, \quad \mathbf{r}_5^x = (0, 0, 0, 0, 0, 1, 0, 0)^\top,$$

$$288 \quad \ell_{1,8}^x = \frac{1}{2c^2} \begin{pmatrix} 0 \\ \mp \hat{\alpha}_f c_f \\ \pm \hat{\alpha}_s c_s \beta_1 \beta_2 \\ \pm \hat{\alpha}_s c_s \beta_1 \beta_3 \\ \frac{1}{\rho} \hat{\alpha}_f \\ 0 \\ \frac{1}{\sqrt{\rho}} \hat{\alpha}_s c \beta_2 \\ \frac{1}{\sqrt{\rho}} \hat{\alpha}_s c \beta_3 \end{pmatrix}, \quad \ell_{2,7}^x = \frac{1}{2} \begin{pmatrix} 0 \\ 0 \\ \mp \beta_3 \\ \pm \beta_2 \\ 0 \\ 0 \\ -\frac{1}{\sqrt{\rho}} \beta_1 \beta_3 \\ \frac{1}{\sqrt{\rho}} \beta_1 \beta_2 \end{pmatrix}, \quad \ell_{3,6}^x = \frac{1}{2c^2} \begin{pmatrix} 0 \\ \mp \hat{\alpha}_s c_s \\ \mp \hat{\alpha}_f c_f \beta_1 \beta_2 \\ \mp \hat{\alpha}_f c_f \beta_1 \beta_3 \\ \frac{1}{\rho} \hat{\alpha}_s \\ 0 \\ -\frac{1}{\sqrt{\rho}} \hat{\alpha}_f c \beta_2 \\ -\frac{1}{\sqrt{\rho}} \hat{\alpha}_f c \beta_3 \end{pmatrix},$$

$$289 \quad \ell_4^x = \left(1, 0, 0, 0, -\frac{1}{c^2}, 0, 0, 0 \right)^\top, \quad \ell_5^x = (0, 0, 0, 0, 0, 1, 0, 0)^\top.$$

Here,

$$(\hat{\alpha}_f, \hat{\alpha}_s) = \begin{cases} \left(\frac{1}{\sqrt{2}}, \frac{1}{\sqrt{2}} \right) & \text{if } b_T = b_3 = 0, \\ \left(\sqrt{\frac{(c^2 - c_s^2)}{(c_f^2 - c_s^2)}}, \sqrt{\frac{(c_f^2 - c^2)}{(c_f^2 - c_s^2)}} \right) & \text{otherwise,} \end{cases}$$

290 and the other notations are the same as in Appendix A. The structure of the matrices T^y and $(T^y)^{-1}$,
291 which diagonalize D^y is similar, but in all of the right and left eigenvectors above, one needs to switch
292 the second and third components as well as the sixth and seventh components.

- [1] D. S. BALSARA, *Divergence-free reconstruction of magnetic fields and WENO schemes for magnetohydrodynamics*, J. Comput. Phys., 228 (2009), pp. 5040–5056.
- [2] D. S. BALSARA, R. KUMAR, AND P. CHANDRASHEKAR, *Globally divergence-free DG scheme for ideal compressible MHD*, Commun. Appl. Math. Comput. Sci., 16 (2021), pp. 59–98.
- [3] D. S. BALSARA AND D. S. SPICER, *A staggered mesh algorithm using high order Godunov fluxes to ensure solenoidal magnetic fields in magnetohydrodynamic simulations*, J. Comput. Phys., 149 (1999), pp. 270–292.
- [4] J. U. BRACKBILL AND D. C. BARNE, *The effect of nonzero $\nabla \cdot \mathbf{B}$ on the numerical solution of the magnetohydrodynamic equations*, J. Comput. Phys., 35 (1980), pp. 426–430.
- [5] M. BRIO AND C. C. WU, *An upwind differencing scheme for the equations of ideal magnetohydrodynamics*, J. Comput. Phys., 75 (1988), pp. 400–422.
- [6] M. J. CASTRO DÍAZ, A. KURGANOV, AND T. MORALES DE LUNA, *Path-conservative central-upwind schemes for non-conservative hyperbolic systems*, ESAIM Math. Model. Numer. Anal., 53 (2019), pp. 959–985.
- [7] P. CHANDRASHEKAR AND C. KLINGENBERG, *Entropy stable finite volume scheme for ideal compressible MHD on 2-D Cartesian meshes*, SIAM J. Numer. Anal., 54 (2016), pp. 1313–1340.
- [8] A. CHERTOCK, S. CHU, M. HERTY, A. KURGANOV, AND M. LUKÁČOVÁ-MEDVID'OVÁ, *Local characteristic decomposition based central-upwind scheme*, J. Comput. Phys., 473 (2023). Paper No. 111718.
- [9] A. CHERTOCK, A. KURGANOV, M. REDLE, AND K. WU, *A new locally divergence-free path-conservative central-upwind scheme for ideal and shallow water magnetohydrodynamics*, SIAM J. Sci. Comput., 46 (2024), pp. A1998–A2024.
- [10] A. CHERTOCK, A. KURGANOV, M. REDLE, AND V. ZEITLIN, *Locally divergence-free well-balanced path-conservative central-upwind schemes for rotating shallow water MHD*, J. Comput. Phys., 518 (2024). Paper No. 113300.
- [11] A. J. CHRISTLIEB, J. A. ROSSMANITH, AND Q. TANG, *Finite difference weighted essentially non-oscillatory schemes with constrained transport for ideal magnetohydrodynamics*, J. Comput. Phys., 268 (2014), pp. 302–325.
- [12] S. CHU, M. HERTY, AND A. KURGANOV, *Novel local characteristic decomposition based path-conservative central-upwind schemes*, J. Comput. Phys., 524 (2025). Paper No. 113692.
- [13] S. CHU AND A. KURGANOV, *Local characteristic decomposition based central-upwind scheme for compressible multi-fluids*, in Finite volumes for complex applications X. Vol. 2. Hyperbolic and related problems, vol. 433 of Springer Proc. Math. Stat., Springer, Cham, 2023, pp. 73–81.
- [14] D. DERIGS, G. J. GASSNER, S. WALCH, AND A. R. WINTERS, *Entropy stable finite volume approximations for ideal magnetohydrodynamics*, Jahresber. Dtsch. Math.-Ver., 120 (2018), pp. 153–219.
- [15] C. R. DEVORE, *Flux-corrected transport techniques for multidimensional compressible magnetohydrodynamics*, J. Comput. Phys., 92 (1991), pp. 142–160.
- [16] M. DUMBSER, D. S. BALSARA, M. TAVELLI, AND F. FAMBRI, *A divergence-free semi-implicit finite volume scheme for ideal, viscous, and resistive magnetohydrodynamics*, Internat. J. Numer. Methods Fluids, 89 (2019), pp. 16–42.
- [17] C. R. EVANS AND J. F. HAWLEY, *Simulation of magnetohydrodynamic flows: A constrained transport method*, Astrophys. J., 332 (1988), pp. 659–677.
- [18] P. FU, F. LI, AND Y. XU, *Globally divergence-free discontinuous Galerkin methods for ideal magnetohydrodynamic equations*, J. Sci. Comput., 77 (2018), pp. 1621–1659.
- [19] T. A. GARDINER AND J. M. STONE, *An unsplit Godunov method for ideal MHD via constrained transport*, J. Comput. Phys., 205 (2005), pp. 509–539.
- [20] S. K. GODUNOV, *Symmetric form of the equations of magnetohydrodynamics (in Russian)*, Numerical Methods for Mechanics of Continuum Medium, 1 (1972), pp. 26–34.
- [21] S. GOTTLIEB, D. KETCHESON, AND C.-W. SHU, *Strong stability preserving Runge-Kutta and multistep time discretizations*, World Scientific Publishing Co. Pte. Ltd., Hackensack, NJ, 2011.
- [22] S. GOTTLIEB, C.-W. SHU, AND E. TADMOR, *Strong stability-preserving high-order time discretization methods*, SIAM Rev., 43 (2001), pp. 89–112.
- [23] C. HELZEL, J. A. ROSSMANITH, AND B. TAETZ, *A high-order unstaggered constrained-transport method for the three-dimensional ideal magnetohydrodynamic equations based on the method of lines*, SIAM J. Sci. Comput., 35 (2013), pp. A623–A651.
- [24] A. KURGANOV, S. NOELLE, AND G. PETROVA, *Semidiscrete central-upwind schemes for hyperbolic conservation laws and Hamilton-Jacobi equations*, SIAM J. Sci. Comput., 23 (2001), pp. 707–740.
- [25] F. LI AND C.-W. SHU, *Locally divergence-free discontinuous Galerkin methods for MHD equations*, J. Sci. Comput., 22/23 (2005), pp. 413–442.
- [26] F. LI AND L. XU, *Arbitrary order exactly divergence-free central discontinuous Galerkin methods for ideal MHD equations*, J. Comput. Phys., 231 (2012), pp. 2655–2675.
- [27] F. LI, L. XU, AND S. YAKOVLEV, *Central discontinuous Galerkin methods for ideal MHD equations with the exactly divergence-free magnetic field*, J. Comput. Phys., 230 (2011), pp. 4828–4847.
- [28] Y. LIU, C.-W. SHU, AND M. ZHANG, *Entropy stable high order discontinuous Galerkin methods for ideal compressible MHD on structured meshes*, J. Comput. Phys., 354 (2018), pp. 163–178.
- [29] S. MISHRA AND E. TADMOR, *Constraint preserving schemes using potential-based fluxes. III. Genuinely multidimensional schemes for MHD equations*, ESAIM Math. Model. Numer. Anal., 46 (2012), pp. 661–680.
- [30] S. A. ORSZAG AND C.-M. TANG, *Small-scale structure of two-dimensional magnetohydrodynamic turbulence*, J. Fluid Mech., 90 (1979), pp. 129–143, <https://doi.org/10.1017/S002211207900210X>.
- [31] K. G. POWELL, *An approximate Riemann solver for magnetohydrodynamics*, in Upwind and High-Resolution Schemes, M. Y. Hussaini, B. van Leer, and J. Van Rosendal, eds., Springer Berlin Heidelberg, Berlin, Heidelberg, 1997, pp. 570–583.
- [32] K. G. POWELL, P. L. ROE, T. J. LINDE, T. I. GOMBOSI, AND D. L. DE ZEEUW, *A solution-adaptive upwind scheme*

- 360 *for ideal magnetohydrodynamics*, J. Comput. Phys., 154 (1999), pp. 284–309.
361 [33] K. G. POWELL, P. L. ROE, R. S. MYONG, T. GOMBOSI, AND D. DE ZEEUW, *An upwind scheme for magnetohydrody-*
362 *namics*, in 12th Computational Fluid Dynamics Conference: AIAA Paper 95-1704-CP, 1995, pp. 661–674.
363 [34] P. L. ROE AND D. S. BALSARA, *Notes on the eigensystem of magnetohydrodynamics*, SIAM J. Appl. Math., 56 (1996),
364 pp. 57–67.
365 [35] J. A. ROSSMANITH, *An unstaggered, high-resolution constrained transport method for magnetohydrodynamic flows*,
366 SIAM J. Sci. Comput., 28 (2006), pp. 1766–1797.
367 [36] G. TÓTH, *The $\nabla \cdot B = 0$ constraint in shock-capturing magnetohydrodynamics codes*, J. Comput. Phys., 161 (2000),
368 pp. 605–652.
369 [37] Z. XU, D. S. BALSARA, AND H. DU, *Divergence-free WENO reconstruction-based finite volume scheme for solving ideal*
370 *MHD equations on triangular meshes*, Commun. Comput. Phys., 19 (2016), pp. 841–880.
371 [38] S. YAKOVLEV, L. XU, AND F. LI, *Locally divergence-free central discontinuous Galerkin methods for ideal MHD*
372 *equations*, J. Comput. Sci., 4 (2013), pp. 80–91.